

Cascaded-Type Band Alignment of a WBG Perovskite/NBG Perovskite For Heterostructure Solar Cells

Anjali Thakran, Anisha Mohapatra, Hemant Verma, Mario Hofmann, Zeeshan Alam Ansari, Chintam Hanmandlu, Chung Hsin Lu, and Chih Wei Chu*



Cite This: ACS Appl. Energy Mater. 2024, 7, 3039–3048



Read Online

ACCESS |

Metrics & More



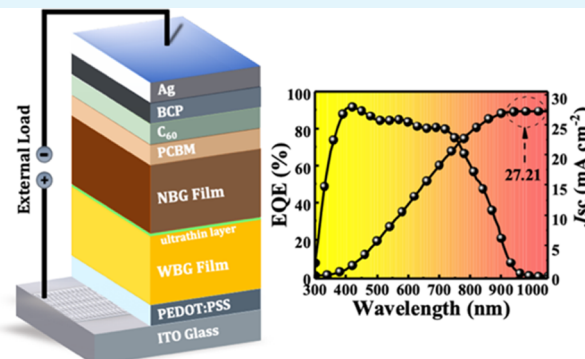
Article Recommendations



Supporting Information

ABSTRACT: The performance of single-junction mixed-halide perovskite-based solar cells is limited by thermalization and spectral losses. With advanced device architectures, the perovskite/perovskite heterostructure, where two or more photoactive layers are stacked together, can help to minimize these losses. In this work, we conformally transfer printed a narrow-band-gap perovskite over a spin-coated wide-band-gap perovskite layer to form a perovskite/perovskite heterostructure. This heterostructure results in broader spectral coverage and the higher position of the lowest unoccupied molecular orbital (LUMO) level of $\text{MAPbBr}_x\text{I}_{3-x}$ compared to $\text{MA}_{0.7}\text{FA}_{0.3}\text{Pb}_{0.5}\text{Sn}_{0.5}\text{I}_3$, forming a cascaded energy level alignment between photoactive layers. Additionally, direct evidence of improved morphology has been observed with the transfer-printing technique in heterostructure formation. The bottom layer provides favorable assistance for the growth of the top perovskite near the interface with good coverage and maintains the quality of the film. Thus, the increased crystallinity and reduced grain boundaries lead to less defects. This reduction played a key role in suppressing recombination losses at the interfaces, ultimately leading to improved device performance. These inherent properties have a positive impact on the photovoltaic response of the device, resulting in broader spectral response and power conversion efficiencies (PCEs) of 14.76% in the heterostructure device. A notable improvement is achieved compared to control single-junction devices, which typically have a PCE of nearly 10% with printed-Sn and 12% with spin-Br-based devices. Moreover, the heterostructure-based device exhibits high stability, retaining almost 80% of its initial PCE value for almost 1000 h with proper encapsulation. Our technique can be utilized for designing low-temperature and solution-processed stacked layers, applicable for optoelectronic devices, including light-emitting diodes (LEDs), sensors, and transistors, where dissolution issues often pose limitations to device architecture.

KEYWORDS: heterostructure, cascaded energy alignment, spin-coated, printed layer, photocarriers, interfaces



INTRODUCTION

Organic/inorganic halide perovskite solar cells (PSCs) have arisen as strong competitors in the photovoltaic market due to their cost-effective processing methods, compatibility with roll-to-roll processing, and high performance.^{1,2} The photoconversion efficiency of the PSCs has steadily increased from 3.8 to 25.6% in single-device architecture.^{3,4} These improvements in photovoltaic performance have been achieved through strategies including composition modification, interfacial and additive engineering, and passivation of perovskite layers.^{6–13} Additionally, advanced device architectures like tandem and heterostructures have been integrated to boost performance, with the latest perovskite/perovskite tandem achieving PCEs of up to 27.4%.⁵ The preference for tandem structures over single-junction configurations is due to their ability to overcome the limitations imposed by the Shockley and Queisser limits. This is achieved by reducing thermal ionization losses and nonabsorption losses, which cannot be

avoided in single-junction PSCs.¹⁴ However, for large-scale production, the tandem structure shows limitations due to their super complex design, including multiple interfaces, choice of the interconnecting layer (ICL), proper current matching conditions, and high-cost deposition methods involved in manufacturing of tandem solar cells.^{15–17}

To address associated challenges with the complex design of tandem structures, a heterostructure is introduced, a junction of two photo-absorbing layers with different band gaps in a simplified device architecture. These architectures imitate tandem structures in terms of their optical and electronic

Received: September 6, 2023

Revised: March 4, 2024

Accepted: March 22, 2024

Published: April 2, 2024



properties and offer more straightforward processing methods and considerable flexibility with solution-based material choices. Thus, this makes them more appealing options for large-area production compared to tandem configuration. In perovskite-based heterostructures, the light-absorbing layers including perovskite/organic, perovskite/quantum dots, perovskite/two-dimensional (2D) wires, and perovskite/perovskite structures have been studied.^{18–22} The perovskite/perovskite structure offers a fascinating approach of optical tunability that enables the stacking of various perovskites with different band gaps (1.2–3.0 eV), resulting in a broader absorption window. Compared with single-junction structures, these structures also help to minimize the transmission and thermalization losses.^{23,24} The heterostructure with perovskite quantum dots (QDs) was previously proposed to relish the importance of the perovskite QDs/perovskite structure with good photovoltaic performance.²⁵ However, challenges in obtaining suitable ligands and producing stable quantum dots for different perovskite-absorption ranges limit their use in stacked devices. Therefore, to create stacked films of different compositions in the heterostructure, some techniques, such as bifacial imprinting, transfer printing, sequential solution vapor deposition, vacuum-assisted deposition, and sequential wet deposition, have been explored in current years.^{26–32} However, the discussed techniques encounter common challenges such as high temperature and long-process time for vacuum-assisted deposition, external pressure requirement for bifacial imprinting, and small-scale fabrication, which is a major concern of these structures. In the fabrication of perovskite/perovskite heterostructures, critical parameters, including solvent selection and annealing conditions, also play a pivotal role in safeguarding the integrity of the subjacent layer.³⁴ Thus, the limited option of fabricating solution-processed photoactive layers may hinder the true potential of these architectures. Therefore, to make stable and high-performance perovskites/perovskite architecture, it is important to come up with an easy-to-use fabrication method that maintains their electrical and optical properties and fully exploits the advantages of heterostructures.

In this study, we have successfully demonstrated a simplified fabrication route that combines a transfer-printed top perovskite layer with another perovskite layer without damaging the underneath layer. A narrow-band-gap perovskite film (printed-Sn) is stacked on top of a wide-band-gap perovskite film (spin-Br) to enhance the spectral response and maximize the utilization of incident photons through device architecture. The presence of cascaded band alignment at the perovskite/perovskite interfaces facilitates the efficient flow of photo-carriers (e–h⁺) throughout the device, resulting in a built-in electric field that promotes faster extraction and transport of charge carriers, ultimately improving the device performance. The trade-off between performance and stability of the heterostructure required good interfacial contact and minimized nonradiative losses. Therefore, we thoroughly discussed the morphology of the perovskite/perovskite heterostructure and reduced interfacial losses through device performance. Our approach of transfer printing enables integration of low-temperature and solution-based materials in stacked architecture, including sensors, light-emitting diodes (LEDs), or other optoelectronic devices.

EXPERIMENTAL SECTION

Materials. The following salts were purchased as mentioned below. Methylammonium bromide (MABr) and methylammonium chloride (MACl) were obtained from Great Cell Solar, and methylammonium iodide (MAI) was purchased from Dyesol. Lead bromide (PbBr_2 , 99.99%) and lead iodide (PbI_2 , 99.99%) were purchased from Alfa Aesar. Tin iodide (SnI_2 , 99%) and tin fluoride (SnF_2 , 99%) were also obtained from the same supplier. Other materials used in this study included 2-hydroxyethyl methacrylate (HEMA, 97%) stabilized with 4-methoxy phenol, PEDOT:PSS (Al4083), and (6,6)-phenyl-C₆₁-butyric acid methyl ester (PCBM), which were all purchased from Sigma-Aldrich. The electron transport layer (ETL) materials 2,9-dimethyl-4,7-diphenyl-1,10-phenanthroline (BCP) and C₆₀ were also obtained from Sigma-Aldrich. The solvents used in our study, including 2-propanol (99.5%), N,N-dimethylformamide (DMF, 99.8%), chlorobenzene (CB, 99.8%), and dimethyl sulfoxide (DMSO, >99.9%), were all purchased from Sigma-Aldrich. All chemicals and solvents were stored in a nitrogen-filled glovebox (with oxygen levels <0.1 ppm) to ensure their quality for an extended period.

Preparation of a Poly(dimethylsiloxane) (PDMS) Stamp. For the preparation of the PDMS stamp, two agents, a Silgard oligomer (SILICONE ELASTOMER, 184 A) and another curing agent, Silgard (SILICONE ELASTOMER, 184 B), were mixed in a fixed ratio (10:1). The mixture was well-blended and placed in a desiccator to remove any air bubbles. The solution was then poured into a glass substrate and heated at 120 °C for 40 min. After cooling, the PDMS stamp was treated with UV-oxygen plasma for 20 min and then immersed in an aqueous solution of HEMA (97%, containing 4-methoxy phenol; Alfa Aesar) for 2 h to uniformly cross-link the monomer units on the surface. The PDMS stamp was subsequently treated with oxygen plasma to create a hydrophilic and smooth surface supported by HEMA. The stamp was stored in a glovebox.

Fabrication of the Device by the Spin-Coating Process. To fabricate the device, a 15 mm × 15 mm piece of indium tin oxide (ITO) glass was cut, etched, and then cleaned with detergent, isopropyl alcohol, and deionized (DI) water (each step lasting 20 min). After the cleaning process, ITO glass was stored in an oven for drying. The glass was treated with UV/ozone for 20 min to clean the surface and improve adhesion for HTL deposition. PEDOT:PSS was spin-coated at 4000 rpm for 30 s as the HTL layer and annealed at 150 °C for 10 min. For the fabrication of the active material, the PEDOT:PSS-coated substrate was placed in a N₂ glovebox (<0.1 ppm, oxygen). The spin-Br perovskite film was made through a two-step interdiffusion process. First, a mixed perovskite precursor of PbBr_2 and PbI_2 was spin-coated at 3000 rpm for 40 s and annealed at 100 °C for 5 min. Then, 80 μL of a mixed organic cation solution (MAI + MABr + MACl) was spin-coated and annealed at 100 °C for 10 min. The film was washed with a 1.5 M MAI solution to remove any residue or unreacted PbI_2 . Subsequently, the PCBM solution was spread onto the active layer using a poly(tetrafluoroethylene) (PTFE) syringe filter (0.45 μm) at 4000 rpm for 40 s. The film was transferred to a thermal deposition chamber, where ETL layers of C₆₀ and BCP were deposited under high vacuum conditions (<10⁻⁶ Pa). Finally, Ag (100 nm) was deposited as contact electrodes using a finger-like mask.

Fabrication of the Device with PDMS Transfer Printing. Initially, the area of the PDMS stamp was maintained in a manner to fully cover the ITO surface area. The perovskite precursor was spread onto the stamp and spin-coated at 4000 rpm for 20 s. The stamp was carefully placed onto the target for transfer printing and quickly removed. The transferred film was washed with an antisolvent (CB) and subjected to annealing at 70 °C for 3 min, followed by 100 °C for 7 min. The remaining steps for device fabrication were performed like the spin-coating process.

Fabrication of the Device by the Sequential Spin and Transfer-Printing Process. A sequential spin and transfer-printing method was used to fabricate a perovskite/perovskite heterostructure film. The bottom layer was produced by using the spin-coating process described earlier. Before adding another layer, a thin layer of

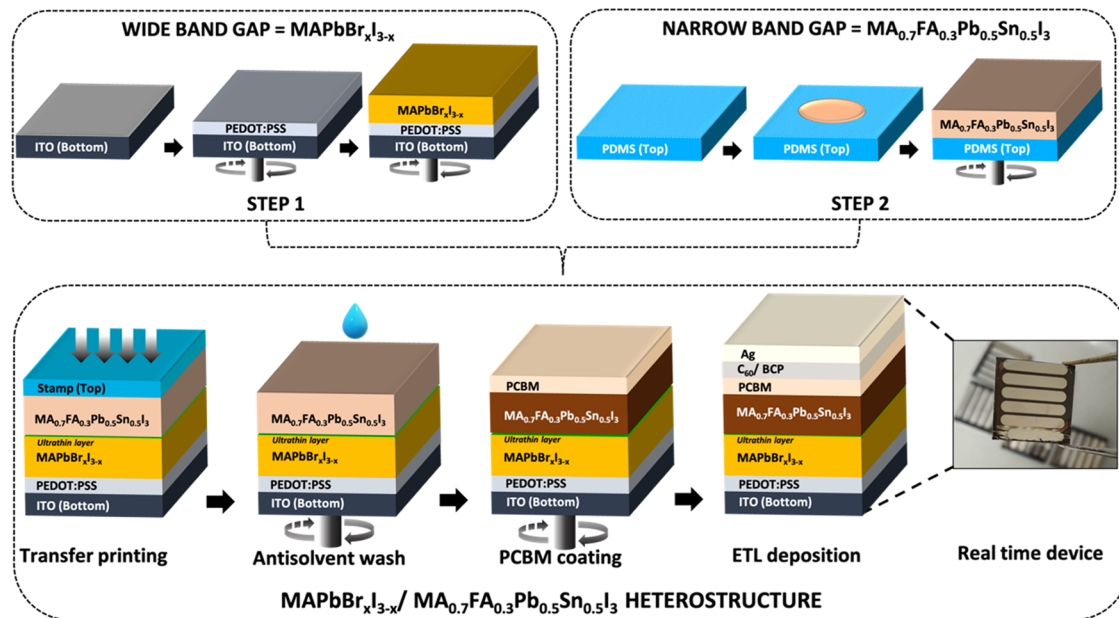


Figure 1. Schematic representation of the WBG perovskite/NBG perovskite heterostructure device. The bottom layer is prepared by the spin-coating (step 1) process, while the top layer is deployed by the PDMS-assisted transfer-printing (step 2) process. The pictorial view of the real-time device is shown in the inset.

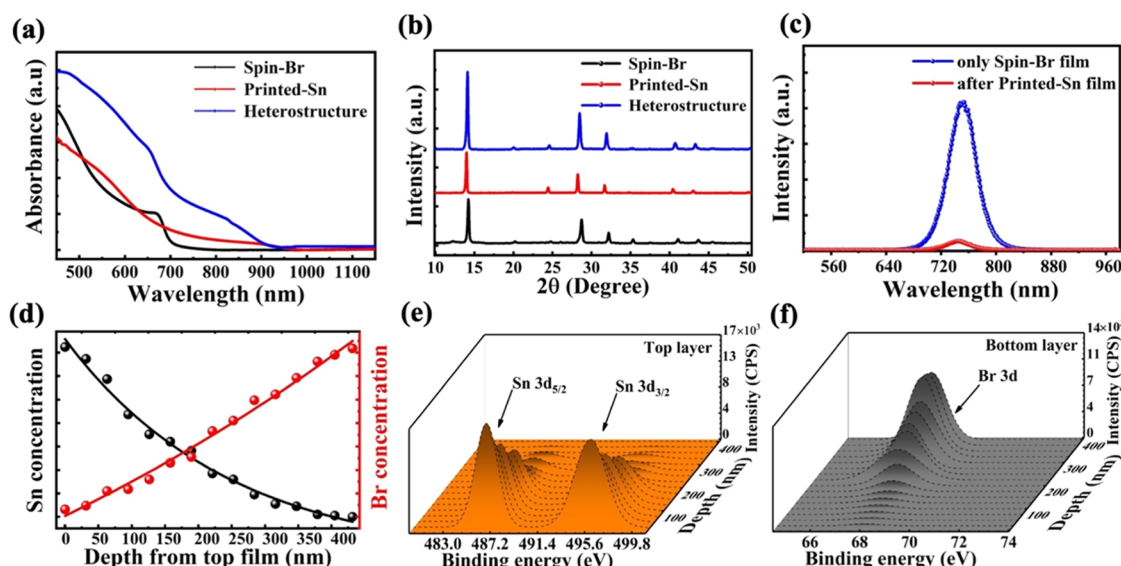


Figure 2. Characterization of spin-Br, printed-Sn, and heterostructure films. (a) Comparison of ultraviolet (UV) absorption spectra for the single-layer spin-Br film (black), the printed-Sn film (red), and the heterostructure (blue). (b) X-ray diffraction spectra of the only spin-Br film, the printed-Sn film, and the heterostructure film. (c) Photoluminescence measurement of the only spin-Br film (blue) and the after printed-Sn film (red) on a prefabricated spin-Br film viewed from the ITO side. The PL was significantly decreased after the printed-Sn film was deployed. (d) Depth profile with atomic composition variation in the heterostructure film. (e) Intensity peaks of Sn 3d_{5/2} and Sn 3d_{3/2} and (f) intensity peaks of Br 3d as a function of depth in the heterostructure.

PCBM was deposited using a spin speed of 7000 rpm for 60 s. Next, the NBG precursor was spread evenly onto a PDMS stamp. The film was then transferred onto the spin-Br film by placing the stamp onto it and immediately peeling it off. The stamp was washed with antisolvent CB and annealed at 70 °C for 3 min and 100 °C for 7 min. The ETL coating was performed as previously described. In this manner, the heterostructure was made through a simple spin-coating and transfer-printing method and later used for analysis.

Characterization. To characterize the prepared film, a suite of techniques was employed. $J-V$ characteristics were recorded using an Agilent 4156C semiconductor parameter analyzer, and a solar simulator (Newport 69920) was calibrated against a standard silicon

photodiode (KG-5 color filter) before any testing. The standard 1-sun conditions (100 mW/cm²) were followed to measure the device, which had an active region of 0.06 cm². External quantum efficiency (EQE) measurements were carried out using an Enlitech EQE system. For the optical study, the film was analyzed on a glass substrate for absorption spectra (Jacob V-670 UV-vis spectrometer), contact angle measurements (Rame-Hart goniometer), and photoluminescence spectra (Attodyne 800, Attocube). The excitation wavelength for the photoluminescence (PL) spectra was a 485 nm laser. For compositional analysis of the surface and depth profile, X-ray photoelectron spectroscopy (XPS, Model PHI 5000 versa probe apparatus) with a 1 kV Ar⁺ ion beam for sputtering was employed. X-ray diffraction

(XRD) measurements were performed using an X-ray diffractometer (PANalytical X'pert PRO) with a Cu K α X-ray tube in the range of 10–50°. For topological analysis, atomic force microscopy (AFM) images were taken with a Bruker Dimension Edge instrument, and scanning electron microscopy (SEM) images were captured with a Carl Zeiss FE-SEM under 10 keV operating conditions. All measurements were performed at room temperature.

RESULTS AND DISCUSSION

A unique fabrication method of perovskite/perovskite architecture is discussed with improved film quality that leads to boosting both the photovoltaic response and stability of the heterostructure device. The schematic of the fabrication procedure is presented in **Figure 1** and also documented in a movie (**Figure S5, Movie 1** in the Supporting Information). The complete device is ITO/PEDOT:PSS/MAPbBr_xI_{3-x}/interlayer/FA_{0.7}MA_{0.3}Pb_{0.5}Sn_{0.5}I₃/PCBM/C₆₀/BCP/Ag. This architecture consists of two photoactive layers, with MAPbBr_xI_{3-x} serving as the bottom layer and FA_{0.7}MA_{0.3}Pb_{0.5}Sn_{0.5}I₃ as the top layer, an inverted (p-i-n) type configuration. The active layer of the heterostructure was fabricated using a two-step process known as sequential spin-coating and the PDMS-assisted stamp-transfer technique. In the first step, the bottom film (spin-Br) was prepared through a spin-coating process. In the second step, the precursor of the top film was coated onto a PDMS stamp. Subsequently, the prepared film on a PDMS stamp was printed onto the bottom film, followed by peeling of the PDMS stamp. The final device architecture of the perovskite/perovskite heterostructure was achieved by depositing the top electrodes. The information on relevant parameters is summarized in the **Experimental Section**. To demonstrate the simplicity of our technique, we also fabricated large-area heterostructure film (3 cm × 3 cm), as shown in **Figure S1a**.

To elucidate the factors contributing to the high performance of this heterostructure, we conducted a comprehensive study of the structure, morphology, and optical properties of a heterostructure-based film and compared it with the single-layer-based film. First, the absorption spectra of the spin-coated WBG perovskite (spin-Br) and the transfer-printed NBG perovskite (printed-Sn) were compared with the heterostructure (stacked NBG/WBG perovskite) film, as illustrated in **Figure 2a**. The spin-Br film showed a shoulder peak at around 725 nm, indicating the absorption of high-energy photons, while the single printed-Sn film showed a peak at around 1000 nm, indicating the absorption of low-energy photons. For the heterostructure film, a shoulder peak at around ~950 nm appeared, which is a contribution of both layers. This also indicates that the top perovskite layer is transferred over the bottom perovskite layer, forming a perovskite/perovskite heterostructure. In addition, compared to the single-layer film, the total absorbance in the heterostructure increased significantly. Later, X-ray diffraction (XRD) analysis was conducted to investigate the structural conformality of the spin-Br, printed-Sn, and heterostructure films, as depicted in **Figure 2b**. The spin-Br-based thin film exhibits peaks at 14.22 and 28.73°, which belong to the 100 and 200 planes,^{33–35} respectively, indicating the formation of a highly crystalline MAPbBr_xI_{3-x} film. A low-intensity peak at around 12.7° indicates the unreacted PbI₂, which can also play a role in surrounding the perovskite grain and therefore provide stability.^{36,37} In the printed-Sn film, the dominant reflection peaks at 14.13 and 28.47°, corresponding to the 100

and 200 planes, respectively, showed similar characteristics as reported in the case of Pb–Sn-based perovskites.^{38,39} The XRD analysis demonstrated that the peaks in the heterostructure film appeared identical to those of a single-layer printed-Sn film, indicating a successful transfer of the top layer. The film showed no peak shift but had a higher peak intensity, indicating a larger crystal size and improved crystallinity. The improved crystallinity was further confirmed by a lower full width of half-maximum (fwhm), which signifies a better film quality. To clearly distinguish the peak position of the spin-Br film and stacked spin-Br/printed-Sn film, we provided enlarged XRD spectra in the Supporting Information (**Figure S2**). The larger crystal size and improved crystallinity of the heterostructure film had a positive impact on the device's performance. Increasing crystal size can greatly reduce the defect density of the bulk layer, thereby minimizing charge trapping and improving exciton dissociation and transport.^{40,41} This observation from scanning electron microscopy (SEM) and atomic force microscopy (AFM) analysis further supported the improved crystal size and better film quality of the heterostructure film. To understand the effect of the transferred top layer (printed-Sn) on the bottom layer (spin-Br), the photoluminescence (PL) of the film was investigated. First, we measured the PL spectra of the single-layer perovskite film [prepared as glass/perovskite (spin-Br)] with an excitation wavelength of 485 nm from the back side of the ITO. Later, we compared this obtained PL with our final device, heterostructure configuration [prepared as the glass/perovskite film (spin-Br)/interlayer/perovskite film (printed-Sn)]. As shown in **Figure 2c**, the PL intensity of only spin-Br (single layer) was higher compared to the stacked film (heterostructure). The decrease in PL intensity indicates the transfer of charge carriers at the perovskite/perovskite interface, which is consistent with reports based on such heterostructure devices.^{42–44} This observation also confirms the successful formation of the perovskite/perovskite heterostructure film.

To further study the stacked architecture, we conducted X-ray photoelectron spectroscopy (XPS) on the surface and depth profiling to determine the elemental composition and distribution of Br and Sn atoms in the heterostructure film. The surface analysis results revealed prominent peaks corresponding to Sn atoms at 484.8 and 493.3 eV (attributed to Sn 3d_{5/2} and Sn 3d_{3/2})³⁸ in the film, while the Br atom peak was negligible, as shown in **Figure S3**. The obtained result indicates that the top surface of the heterostructure film was primarily composed of the printed-Sn layer. To identify the presence of Br atoms and investigate ion diffusion at the interfaces of MAPbBr_xI_{3-x}/FA_{0.7}MA_{0.3}Pb_{0.5}Sn_{0.5}I₃, we performed depth profiling measurements using Ar ion sputtering (1 keV energy), as shown in **Figure 2d**. The concentration of Sn atoms was found to be higher on the top surface and gradually decreased with thickness toward the bottom layer. Conversely, the presence of Br atoms increased as the sputtering process reached the bottom layer. This variation in peak intensity with the depth in the stacked structure indicates that the top layer is predominantly composed of Sn atoms, while the bottom layer exhibits behavior dominated by Br atoms. The results obtained from ion sputtering are plotted in a three-dimensional (3D) view in **Figure 2e,f**, which shows the intensity variation of Sn and Br atoms with the depth of the film. On the top surface, the peak intensity of Sn atoms was higher and gradually decreased toward the bottom, whereas the intensity of Br atoms was lower on the surface and

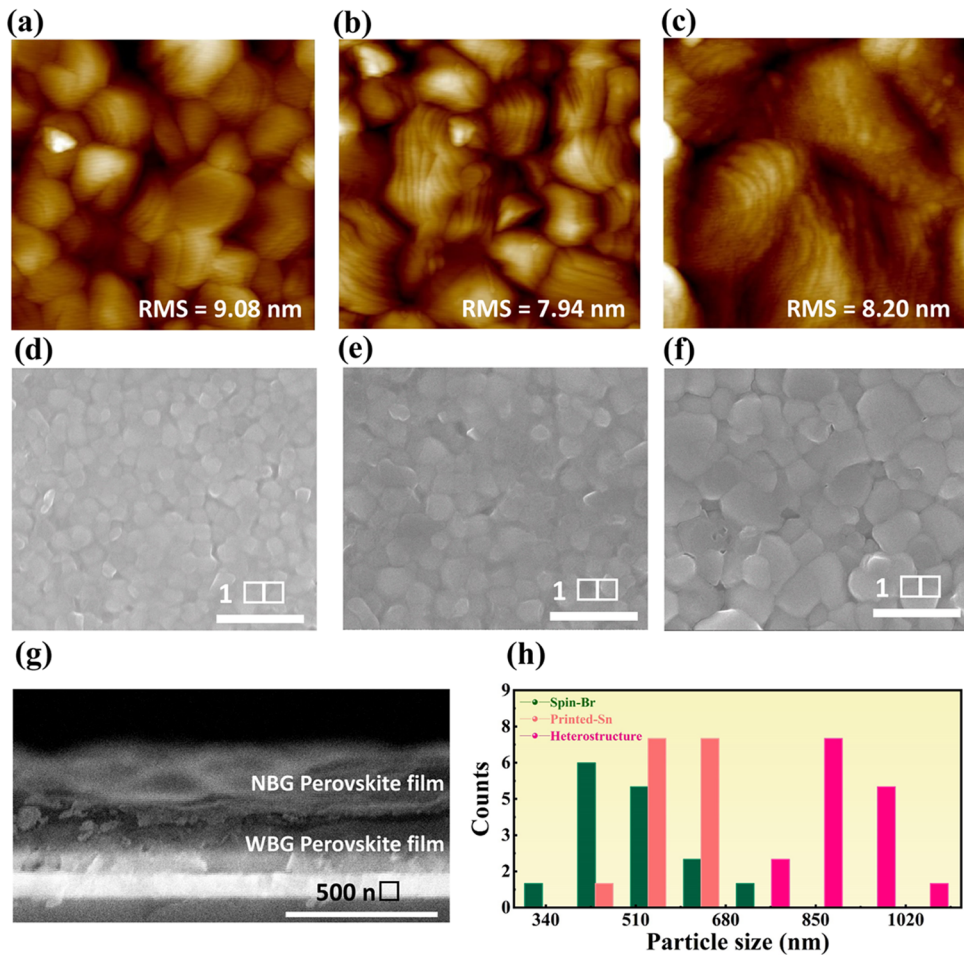


Figure 3. Morphology analysis of films. (a–c) AFM images of the spin-Br film, the printed-Sn film, and the heterostructure film (top view) on a glass substrate. (d–f) SEM images of all three films at a 1 μm scale bar. (g) Cross-sectional SEM image of the heterostructure. (h) Average particle size distribution for the corresponding films.

gradually increased toward the bottom. A small presence of both atoms was observed at the interface of the Br-rich and Sn-rich films, possibly due to diffusion at the interface. However, the distinct behavior is more prominent on the top or bottom surfaces. The peak positions on the surface were also verified in single-layer spin-Br and printed-Sn films. Clear and sharp peaks attributed to Br 3d (67.02 eV), Pb 4f_{7/2} and 4f_{5/2} (136.6 and 141.4 eV), and I 3d_{5/2} and I 3d_{3/2} (618.4 and 629.7 eV) were observed, indicating a good film formation, as shown in Figure S3a–f.^{45–47}

To investigate the film morphology, we performed AFM and SEM analyses of the spin-Br, printed-Sn, and stacked heterostructure thin films. The AFM study revealed that all three films exhibited a smooth and uniform surface, as shown in Figure 3a–c, with similar root-mean-square (RMS) roughness values of 9.08, 7.94, and 8.20 nm for spin-Br, printed-Sn, and heterostructure thin films, respectively. The lower roughness value of the heterostructure film indicated the formation of a smooth surface due to good interfacial contact between the printed-Sn film over the spin-Br film. The morphology of films was further confirmed by SEM top view images shown in Figure 3d–f. Among the three films, the heterostructure film exhibited improved crystallinity, larger grain size, and fewer grain boundaries. The average particle size of the spin-Br film, printed-Sn film, and heterostructure film was calculated as 520, 580, and 850 nm, respectively, as shown

in Figure 3h. The significantly increased grain size in the heterostructure film was attributed to an improved crystallization process influenced by the presence of an underlying perovskite layer (spin-Br film).^{29,48,49} This observation indicated the good compatibility of the top perovskite layer with the bottom perovskite layer, forming a cascaded-type heterostructure. Moreover, the larger crystals in the heterostructure film with fewer grain boundaries effectively reduced trap states on the surfaces, therefore minimizing recombination losses. To check the uniformity of the heterostructure film, SEM images were taken at various spots, revealing no pinholes in the thin film. This further provided evidence for a uniform heterostructure film over the active region (see Supporting Information, Figure S5). The improved morphology of the heterostructure film may contribute to the enhanced photovoltaic performance of the device. The cross-sectional view displayed in Figure 3g showed that the total thickness of the heterostructure film is approximately 400 nm. The heterostructure device architecture, consisting of ITO/PEDOT:PSS/MAPbBr_xI_{3-x}/ultrathin layer/FA_{0.7}MA_{0.3}Pb_{0.5}Sn_{0.5}I₃/PCBM/C₆₀/BCP/Ag, was fabricated, as displayed in Figure 4a. An ultrathin PCBM layer was applied to avoid diffusion at the interface. The ultrathin PCBM acted as a barrier layer and helped in passivating any voids/trap states^{50,51} on the prefabricated spin-Br-based layer. The band alignment is an important factor for the suitable flow of electrons and holes

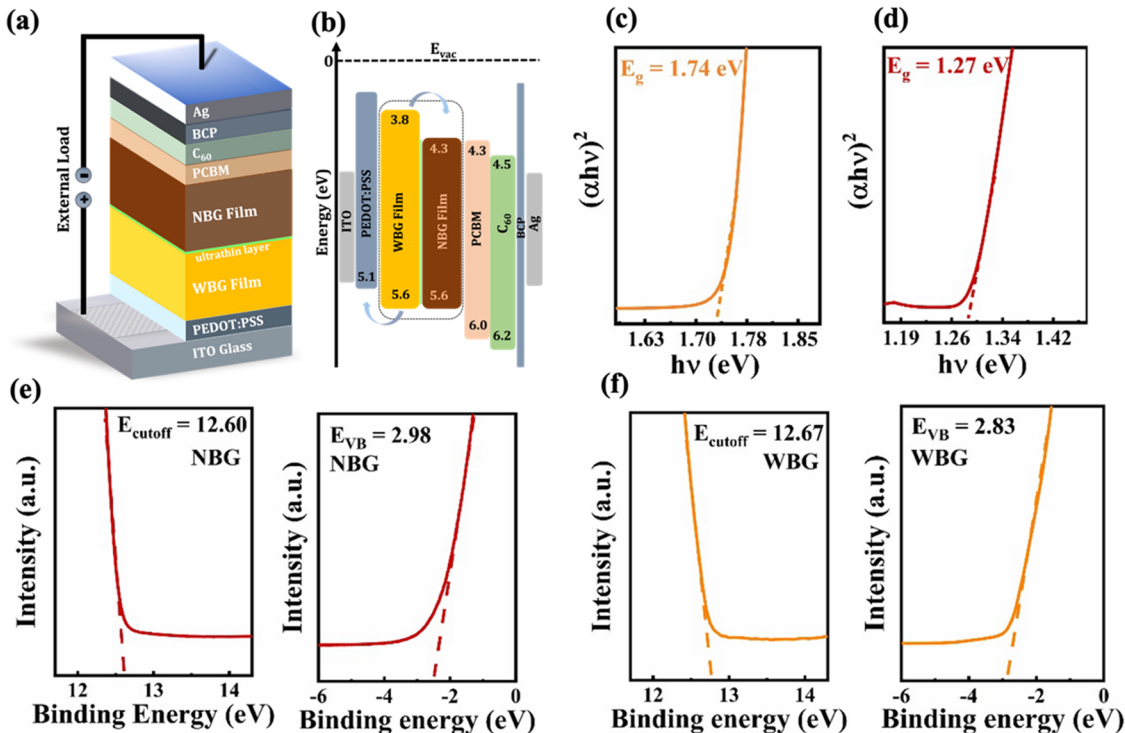


Figure 4. (a) Schematic diagram of heterostructure device architecture. (b) Schematic illustration of energy level alignment in the heterostructure. (c) Optical band of the spin-Br film (orange) and the printed-Sn film (maroon) through Tauc plot calculation. (d) Secondary electron cutoff region (E_{cutoff}) and the valence band top region (E_{VB}) of spin-Br and printed-Sn films.

(photocarriers) throughout the device. Therefore, we investigated the possible energy level alignment among the active layers. The device energy band diagram is schematically depicted in Figure 4b, and the energy levels of the photoactive layer were confirmed by photoemission spectroscopy and UV-absorption data. The optical band gaps of the active layers were calculated through Tauc plot calculations, as illustrated in Figure 4c. Our results showed that the spin-Br layer had an optical band gap of 1.74 eV and the printed-Sn layer had an optical band gap of 1.27 eV. Ultraviolet photoemission spectroscopy (UPS) measurements were conducted to determine the Fermi level (E_F) and valence band maxima positions of the spin-Br and printed-Sn films. The values were calculated using Einstein's photoemission law ($E_F = h\nu - E_{\text{cutoff}}$), where $h\nu$ is the photon energy (21.22 eV) and E_{cutoff} is the limiting edge for secondary electrons.^{52,53} The results showed that the conduction band position (CB)/valence band position (VB) of the spin-Br perovskite was $-3.86/-5.60$ eV and that of the printed-Sn perovskite was $-4.33/-5.60$ eV, respectively, as displayed in Figure 4d. Due to the different elemental compositions of the films (as confirmed by XRD and XPS analyses), the CB positions of the respective perovskite materials showed variations. The higher CB position of the spin-Br film compared to that of the printed-Sn film is beneficial for the transfer of photoelectrons from spin-Br to printed-Sn. In a stacked architecture, this allows for a large flux of photogenerated carriers to flow from the active materials to the respective electrodes. Furthermore, the smaller energy offset between the photoactive materials can create a built-in electric field at the interfaces, leading to faster carrier extraction.⁴⁵ Thus, the alignment of the band ensures a smooth flow of carriers within the device, resulting in improved device performance.

The current density–voltage (J – V) characteristics of the best-performing single-layer spin-Br-based PSCs, single-layer printed-Sn-based PSCs, and heterostructure-based PSCs are displayed in Figure 5a. To achieve an efficient perovskite/perovskite heterostructure, we initially evaluated the device performance of spin-Br and printed-Sn films in a single-junction architecture. The best-performing spin-Br-based device exhibited a power conversion efficiency (PCE) of 12.43%, an open-circuit voltage (V_{oc}) of 1.02 V, and a short-circuit current density (J_{sc}) of 18.10 mA/cm^2 with a fill factor (FF) of 67.33%. Likewise, the best-performing printed-Sn-based device exhibited a PCE of 10.96%, a V_{oc} of 0.65 V, a J_{sc} of 27.56 mA/cm^2 , and an FF of 61.08%. Further information related to these single-junction devices can be found in the Supporting Information (Figure S6). The V_{oc} values of the single-layer printed-Sn, single-layer spin-Br, and the heterostructure were 0.65, 1.02, and 0.81 V, respectively. Interestingly, an improvement in V_{oc} is observed in the heterostructure compared with the single-junction printed-Sn device. The improved V_{oc} of the heterostructure device is the contribution of both the top and bottom layers. Apart from V_{oc} improvement, we also noted a consistent J_{sc} enhancement in the heterostructure device through J – V measurement as well as EQE measurement. The value of J_{sc} in spin-Br-based PSCs is $\sim 18 \text{ mA/cm}^2$, printed-Sn-based PSCs is $\sim 27 \text{ mA/cm}^2$, and heterostructure-based PSCs is $\sim 28 \text{ mA/cm}^2$. This improvement in J_{sc} is due to the presence of both photoactive layers, which leads to an increase in the number of photocarriers in heterostructure architecture. Moreover, the integration of two photoactive layers with different band gaps also helps to minimize losses, thereby improving performance. To further demonstrate the improvement of J_{sc} in heterostructure-based PSCs, we performed an EQE measurement on the best device.

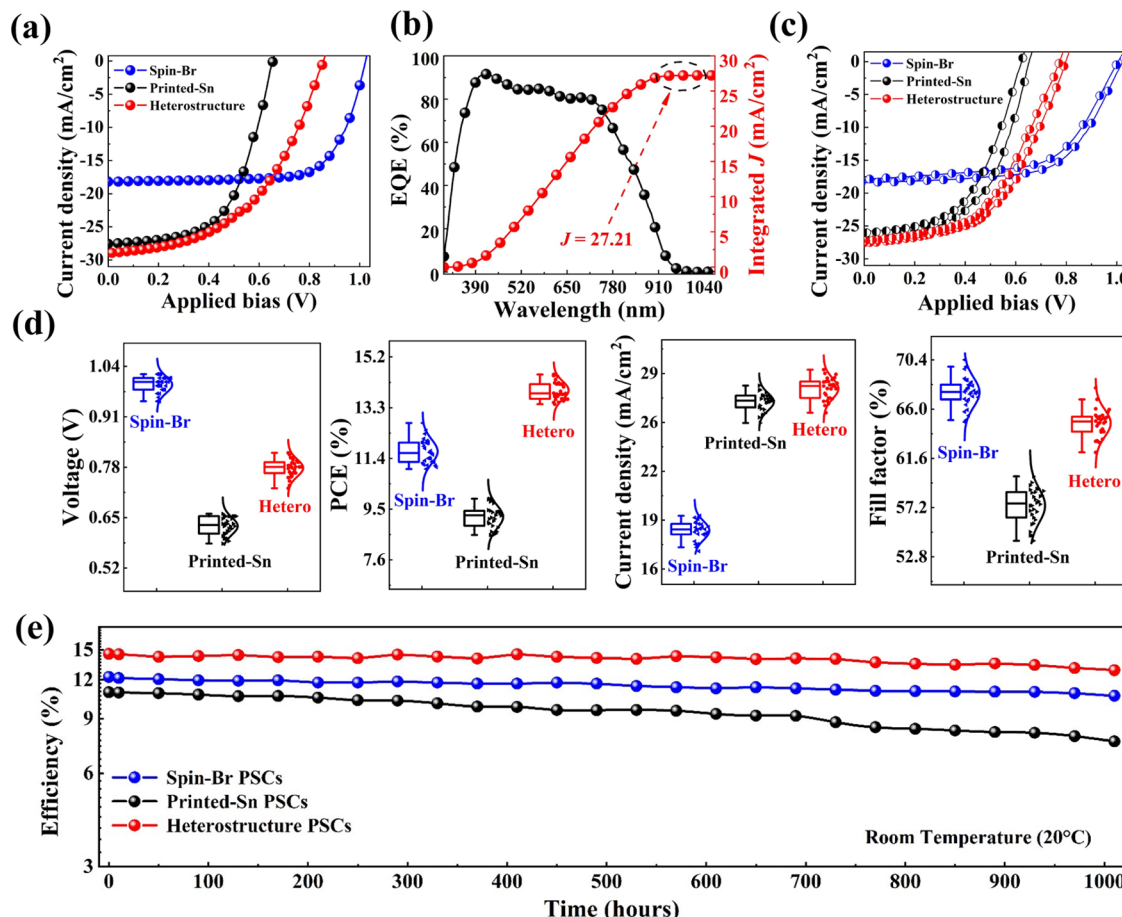


Figure 5. (a) Current density–voltage ($J-V$) characteristics of single-layer spin-Br (blue), single-layer printed-Sn (black), and heterostructure (red) devices. (b) EQE spectra of the heterostructure with integrated current density. (c) $J-V$ analysis with forward and reverse scans of all three devices. (d) Comparison of PV performance with statistical distribution data. (e) Stability test of the spin-Br PSCs, printed-Sn PSCs, and heterostructure PSCs stored in a N_2 -filled glovebox.

As shown in Figure 5b, with the printed-Sn layer on the spin-Br layer, we obtained an extended spectral response up to approximately 950 nm, whereas it was limited to around 725 nm with the spin-Br layer alone. This improved spectral response provides further evidence of the contribution of both photoactive layers. We also calculated the integrated J_{sc} in the heterostructure, which was found to be 27.21 mA/cm², consistent with the improved J_{sc} observed in the $J-V$ measurement. This further highlights the importance of the heterostructure in improving the collection probability of photocarriers for an extended wavelength. Figure 5c presents the forward and reverse scan of the best-performing device in typical $J-V$ measurements. It is worth noting that the printed-Sn layer in heterostructure formation showed less hysteresis compared to the only printed-Sn layer in single-device architecture. The optimal heterostructure device achieved an FF of 64% through the transfer-printing process. This could be due to improved crystallinity and reduced grain boundaries, as confirmed through AFM and SEM analyses.

In addition, we studied the effect of varying the thickness of the active layer on device performance, as presented in Figure S7. A thicker active layer region resulted in a higher current density value due to enhanced light absorption; however, it led to a lower V_{oc} value as the charge carriers had to travel a longer distance before recombination. On the other hand, a thinner layer led to a lower photocurrent value due to insufficient

photon absorption.⁵⁵ We found that an optimal thickness of approximately 400 nm in heterostructure PSC films provided the best balance between J_{sc} and V_{oc} . The statistical distribution of photovoltaic parameters (V_{oc} , J_{sc} , PCE, and FF) of spin-Br, printed-Sn, and heterostructure films is plotted in Figure 5d. Remarkably, the champion performance of heterostructure PSCs exhibited a V_{oc} of 0.81 V, a J_{sc} of 28.26 mA/cm², FF of 64.48%, and PCEs of 14.76%. The current density from $J-V$ and EQEs measurements has been compared in the Supporting Information (Table S2). The obtained results showed that heterostructure-based PSCs had better performance than single-layer spin-Br- or printed-Sn-based PSCs. We attribute the remarkable performance of the heterostructure to extended absorption through the printed-Sn layer onto the spin-Br layer, which enables the absorption of photons from the visible to the NIR region. This greatly helps minimize spectral losses. Additionally, proper band alignment can significantly reduce carrier recombination, voltage deficits, and trap states into stacked architecture.^{54,55} We confirmed the smooth transfer of charge carriers at the interfaces in the heterostructure with proper band alignment. Also, the quenching of PL also ensures the proper stacking of the layers. The heterostructure PSCs showed higher device performance with a PCE of ~15%, compared to the single spin-Br PSCs (~12%) and single printed-Sn PSCs (~10%). The average and champion performance of single and

Table 1. Device Metrics of Single Spin-Br, Printed-Sn, and Heterostructure PSC are Summarized

device structure	type	J_{sc} (mA/cm ²)	V_{oc} (V)	FF (%)	PCE (%)
MAPbBr _x I _{3-x} (single)	average	17.89	1.00	64.05	11.46
	champion	18.10	1.02	67.33	12.43
MA _{0.7} FA _{0.3} Pb _{0.5} Sn _{0.5} I ₃ (single)	average	27.11	0.64	58.38	10.13
	champion	27.56	0.65	61.08	10.94
MAPbBr _x I _{3-x} /MA _{0.7} FA _{0.3} Pb _{0.5} Sn _{0.5} I ₃ (heterostructure)	average	28.06	0.79	61.46	13.62
	champion	28.26	0.81	64.48	14.76

heterostructure devices is compared in Table 1, confirming the excellent reproducibility and repeatability of the fabricated devices in both device architectures. We also conducted stability tests of single spin-Br PSCs, printed-Sn PSCs, and heterostructure PSCs, as shown in Figure 5e. All of the devices were encapsulated with polyamide tape for EQE measurements, and the heterostructure showed relatively stable performance. Further, the stability of the best-performing heterostructure device was studied at continuous illumination (AM 1.5G) under 25 ± 5 °C. The heterostructure devices exhibited consistent performance over the 300 s testing period while retaining both the fill factor (FF) and current density (J_{sc}) with maintained power conversion efficiency (PCE), as provided in Figure S9. The devices were stored in a nitrogen-filled glovebox after each measurement. Additionally, we performed a thermal stability test of heterostructure devices at varying temperatures from 60 to 100 °C (Figure S7c). The device was heated in a glovebox for 10 min and cooled for measurement. The heterostructure showed degradation when exposed to high temperatures, but the heterostructure at room temperature maintained long-term stability over 1000 h. With the importance of broadening the light spectrum, our heterostructure design with a cascade-type band alignment showed a good response. Furthermore, the limited literature on solution-based stacked architecture makes our fabrication route of interest for use in other practical applications.

CONCLUSIONS

In summary, we have successfully demonstrated the fabrication of a WBG perovskite/NBG perovskite heterostructure through a simple sequential spin and transfer-printing process. The heterostructure showed a remarkable improvement in PCE compared to single-junction device, reaching the highest value of 14.76% due to defect passivation and improved charge extraction in device architecture. The enhanced performance of heterostructured devices can be attributed to several factors. First, the combination of two different band-gap materials broadens light coverage through device architecture, leading to better photocarrier generation throughout the device. Second, the presence of cascaded band alignment between the two photoactive layers facilitates the effective transfer of photocarriers. Lastly, reducing grain boundaries and defects across the interface leads to improved crystallinity of the heterostructure film. Therefore, our low-temperature and solution-based deposition technique provides a cost-effective and compatible pathway for designing a perovskite/perovskite heterostructure, which can be used for other optoelectronic devices. This approach holds significant potential for competing with other fabrication techniques in terms of performance and stability.

ASSOCIATED CONTENT

Supporting Information

The Supporting Information is available free of charge at <https://pubs.acs.org/doi/10.1021/acsaem.3c02258>.

Top layer transfer printed on the prefabricated bottom layer (Figure S5) (Movie 1) ([MOV](#))

Photographic representation of the large-scale fabricated heterostructure film, magnified view of XRD spectra of the spin-Br and heterostructure perovskite film, XPS spectra of single-layer spin-Br and printed-Sn films, surface examination of the heterostructure at multiple spots, illustration of heterostructure design, fabrication process demonstration video, EQE measurement for spin-Br and printed-Sn perovskite films, EQE and thickness dependence analysis of the heterostructure, thermal stability test, and comparison of the current density of J-V and EQE measurement ([PDF](#))

AUTHOR INFORMATION

Corresponding Author

Chih Wei Chu – Research Center for Applied Sciences, Academia Sinica, Taipei 11529, Taiwan ROC; Department of Photonics, National Yang Ming Chiao Tung University, Hsinchu City 30010, Taiwan ROC; College of Engineering, Center for Green Technology, Chang Gung University, Taoyuan City 333002, Taiwan ROC; Present Address: Research Center for Applied Science, Academia Sinica, Nangang, Academia Rd, 115024, Taipei 115, Taiwan ROC; orcid.org/0000-0003-0979-1729; Email: gchu@gate.sinica.edu.tw

Authors

Anjali Thakran – Department of Physics, National Taiwan University, Taipei 106, Taiwan ROC; Research Center for Applied Sciences, Academia Sinica, Taipei 11529, Taiwan ROC; Nano-Science and Technology Program, Taiwan International Graduate Program, Academia Sinica, Taipei 106, Taiwan ROC; orcid.org/0000-0003-1250-2166

Anisha Mohapatra – Research Center for Applied Sciences, Academia Sinica, Taipei 11529, Taiwan ROC

Hemant Verma – Department of Physics, National Taiwan University, Taipei 106, Taiwan ROC

Mario Hofmann – Department of Physics, National Taiwan University, Taipei 106, Taiwan ROC; orcid.org/0000-0003-1946-2478

Zeeshan Alam Ansari – Department of Physics, National Taiwan University, Taipei 106, Taiwan ROC

Chintam Hanmandlu – Research Center for Applied Sciences, Academia Sinica, Taipei 11529, Taiwan ROC

Chung Hsin Lu – Department of Chemical Engineering, National Taiwan University, Taipei 106, Taiwan ROC

Complete contact information is available at:

<https://pubs.acs.org/10.1021/acsaem.3c02258>

Author Contributions

C.W.C. directed and monitored the project. A.T. fabricated the device and A.M. assisted during the experiment. H.V. performed XPS measurements and Z.A.A. assisted in AFM measurements. A.T. performed and analyzed the SEM characterization. M.H. provided valuable comments to organize the manuscript. A.M., M.H., C.H.L., C.H., and C.W.C. commented on the manuscript. All authors participated in the writing and discussion of this manuscript.

Notes

The authors declare no competing financial interest.

ACKNOWLEDGMENTS

Dr. C.W.C. thanks the National Science and Technology Council—Taiwan (NSTC 111-2221-E-001-006) and the National Taiwan University and Academia Sinica Innovative Joint Program (NTU-AS-112L104307) for the essential financial support. The authors are also grateful to the Research Center for Applied Sciences at Academia Sinica and the Department of Physics at National Taiwan University for the resources provided to conduct their research work. A.T. sincerely acknowledges the Taiwan International Graduate Program (TIGP-NANO) for providing professional development opportunities to pursue her research work.

ABBREVIATIONS

WBG, wide band gap; NBG, narrow band gap; PCEs, power conversion efficiencies; EQE, external quantum efficiency; FF, fill factor; J_{sc} , short-circuit current density; V_{oc} , open-circuit voltage; XRD, X-ray diffraction; PDMS, poly(dimethylsiloxane); AFM, atomic force microscopy; SEM, scanning electron microscopy; XPS, X-ray photoemission spectroscopy; PL, photoluminescence; XPS, X-ray photoemission spectroscopy; UPS, ultraviolet photoemission spectroscopy

REFERENCES

- (1) Ma, Y.; Zhao, Q. A strategic review on processing routes towards scalable fabrication of perovskite solar cells. *J. Energy Chem.* **2022**, *64*, 538–560.
- (2) Wu, X.; Li, B.; Zhu, Z.; Chueh, C. C.; Jen, A. K. Y. Designs from single junctions, heterojunctions to multijunctions for high-performance perovskite solar cells. *Chem. Soc. Rev.* **2021**, *50* (23), 13090–13128.
- (3) Kojima, A.; Teshima, K.; Shirai, Y.; Miyasaka, T. Organometal halide perovskites as visible-light sensitizers for photovoltaic cells. *J. Am. Chem. Soc.* **2009**, *131*, 6050–6051.
- (4) National Renewable Energy Lab. Best Research-Cell Efficiency Chart. <https://www.nrel.gov/pv/cell-efficiency.html> (2022).
- (5) Chen, H.; Maxwell, A.; Li, C.; Teale, S.; Chen, B.; Zhu, T.; Ugur, E.; Harrison, G.; Grater, L.; Wang, J.; Wang, Z.; et al. Regulating surface potential maximizes voltage in all-perovskite tandems. *Nature* **2023**, *613* (7945), 676–681.
- (6) Park, N. G. Perovskite solar cells: an emerging photovoltaic technology. *Mater. Today* **2015**, *18* (2), 65–72.
- (7) Hao, M.; Bai, Y.; Zeiske, S.; Ren, L.; Liu, J.; Yuan, Y.; Zarrabi, N.; Cheng, N.; Ghasemi, M.; Chen, P.; Lyu, M.; He, D.; Yun, J. H.; Du, Y.; Wang, Y.; Ding, S.; Armin, A.; Meredith, P.; Liu, G.; Cheng, H. M.; Wang, L. Ligand-assisted cation-exchange engineering for high-efficiency colloidal $\text{Cs}_1\text{xFAxPbI}_3$ quantum dot solar cells with reduced phase segregation. *Nat. Energy* **2020**, *5*, 79–88.
- (8) Zhou, H.; Chen, Q.; Li, G.; Luo, S.; Song, T. B.; Duan, H. S.; Hong, Z.; You, J.; Liu, Y.; Yang, Y. Interface engineering of highly efficient perovskite solar cells. *Science* **2014**, *345*, 542–546.
- (9) Yang, W. S.; Park, B. W.; Jung, E. H.; Jeon, N. J.; Kim, Y. C.; Lee, D. U.; Shin, S. S.; Seo, J.; Kim, E. K.; Noh, J. H.; Seok, S. I. Iodide management in formamidinium-lead-halide-based perovskite layers for efficient solar cells. *Science* **2017**, *356*, 1376–1379.
- (10) Saliba, M.; Matsui, T.; Domanski, K.; Seo, J. Y.; Ummadisingu, A.; Zakeeruddin, S. M.; Correa-Baena, J. P.; Tress, W. R.; Abate, A.; Hagfeldt, A.; Grätzel, M. Incorporation of rubidium cations into perovskite solar cells improves photovoltaic performance. *Science* **2016**, *354*, 206–209.
- (11) Adjokatse, S.; Fang, H. H.; Loi, M. A. Broadly tunable metal halide perovskites for solid-state light-emission applications. *Mater. Today* **2017**, *20*, 413–424.
- (12) Wang, Q.; Shao, Y.; Dong, Q.; Xiao, Z.; Yuan, Y.; Huang, J. Large fill-factor bilayer iodine perovskite solar cells fabricated by a low-temperature solution-process. *Energy Environ. Sci.* **2014**, *7* (7), 2359–2365.
- (13) Zhou, H.; Chen, Q.; Li, G.; Luo, S.; Song, T. B.; Duan, H. S.; Hong, Z.; You, J.; Liu, Y.; Yang, Y. Interface engineering of highly efficient perovskite solar cells. *Science* **2014**, *345*, 542–546.
- (14) Shockley, W.; Queisser, H. J. Detailed balance limit of efficiency of p-n junction solar cells. *J. Appl. Phys.* **1961**, *32*, 510–519.
- (15) Sha, W. E. I.; Ren, X.; Chen, L.; Choy, W. C. The efficiency limit of $\text{CH}_3\text{NH}_3\text{PbI}_3$ perovskite solar cells. *Appl. Phys. Lett.* **2015**, *106*, No. 221104.
- (16) Jaysankar, M.; Raul, B. A.; Bastos, J.; Burgess, C.; Weijtens, C.; Creatore, M.; Aernouts, T.; Kuang, Y.; Gehlhaar, R.; Hadipour, A.; Poortmans, J. Minimizing voltage loss in wide-bandgap perovskites for tandem solar cells. *ACS Energy Lett.* **2019**, *4*, 259–264.
- (17) Hadipour, A.; De Boer, B.; Blom, P. W. M. Solution-processed organic tandem solar cells with embedded optical spacers. *J. Appl. Phys.* **2007**, *102* (7), No. 074506, DOI: [10.1063/1.2786024](https://doi.org/10.1063/1.2786024).
- (18) Futscher, M. H.; Ehrler, B. Efficiency limit of perovskite/Si tandem solar cells. *ACS Energy Lett.* **2016**, *1* (4), 863–868.
- (19) Chiang, C. H.; Wu, C. G. Bulk heterojunction perovskite-PCBM solar cells with high fill factor. *Nat. Photonics* **2016**, *10* (3), 196–200.
- (20) Grancini, G.; Roldán-Carmona, C.; Zimmermann, I.; Mosconi, E.; Lee, X.; Martineau, D.; Narbey, S.; Oswald, F.; De Angelis, F.; Graetzel, M.; Nazeeruddin, M. K. One-Year stable perovskite solar cells by 2D/3D interface engineering. *Nat. Commun.* **2017**, *8* (1), No. 15684.
- (21) Eperon, G. E.; Stranks, S. D.; Menelaou, C.; Johnston, M. B.; Herz, L. M.; Snaith, H. J. Formamidinium lead trihalide: a broadly tunable perovskite for efficient planar heterojunction solar cells. *Energy Environ. Sci.* **2014**, *7*, 982–988.
- (22) Wang, C.; Zhao, Y.; Ma, T.; An, Y.; He, R.; Zhu, J.; Chen, C.; Ren, S.; Fu, F.; Zhao, D.; Li, X. A universal close-space annealing strategy towards high-quality perovskite absorbers enabling efficient all-perovskite tandem solar cells. *Nat. Energy* **2022**, *7* (8), 744–753.
- (23) Zhao, D.; Chen, C.; Wang, C.; Junda, M. M.; Song, Z.; Grice, C. R.; Yu, Y.; Li, C.; Subedi, B.; Podraza, N. J.; Zhao, X.; Fang, G.; Xiong, R. G.; Zhu, K.; Yan, Y. Efficient two-terminal all-perovskite tandem solar cells enabled by high-quality low-bandgap absorber layers. *Nat. Energy* **2018**, *3* (12), 1093–1100.
- (24) Zhao, Q.; Hazarika, A.; Chen, X.; Harvey, S. P.; Larson, B. W.; Teeter, G. R.; Liu, J.; Song, T.; Xiao, C.; Shaw, L.; Zhang, M.; Li, G.; Beard, M. C.; Luther, J. M. High efficiency perovskite quantum dot solar cells with charge separating heterostructure. *Nat. Commun.* **2019**, *10*, No. 2842, DOI: [10.1038/s41467-019-10856-z](https://doi.org/10.1038/s41467-019-10856-z).
- (25) Mohapatra, A.; Singh, N.; Singh, A.; Lee, C. Y.; Lu, Y. J.; Tao, Y. T.; Lee, C. H.; Chu, C. W. Solution-processed perovskite/perovskite heterostructure via a grafting-assisted transfer technique. *ACS Appl. Energy Mater.* **2021**, *4* (2), 1962–1971.
- (26) Dänkamp, B.; Müller, C.; Sendner, M.; Boix, P. P.; Sessolo, M.; Lovrincic, R.; Bolink, H. J. Perovskite–perovskite homojunctions

- via compositional doping. *J. Phys. Chem. Lett.* **2018**, *9* (11), 2770–2775.
- (27) Clark, C. P.; Mann, J. E.; Bangsund, J. S.; Hsu, W. J.; Aydil, E. S.; Holmes, R. J. Formation of Stable Metal Halide Perovskite/Perovskite Heterojunctions. *ACS Energy Lett.* **2020**, *5* (11), 3443–3451.
- (28) Liu, Y.; Hong, Z.; Chen, Q.; Chang, W.; Zhou, H.; Song, T. B.; Young, E.; Yang, Y.; You, J.; Li, G.; Yang, Y. Integrated perovskite/bulk-heterojunction toward efficient solar cells. *Nano Lett.* **2015**, *15* (1), 662–668.
- (29) Yang, X.; Li, Q.; Zheng, Y.; Luo, D.; Zhang, Y.; Tu, Y.; Zhao, L.; Wang, Y.; Xu, F.; Gong, Q.; Zhu, R. Perovskite hetero-bilayer for efficient charge-transport-layer-free solar cells. *Joule* **2022**, *6* (6), 1277–1289.
- (30) Kang, D. H.; Kim, S. G.; Kim, Y. C.; Han, I. T.; Jang, H. J.; Lee, J. Y.; Park, N. G. CsPbBr₃/CH₃NH₃PbCl₃ double layer enhances efficiency and lifetime of perovskite light-emitting diodes. *ACS Energy Lett.* **2020**, *5* (7), 2191–2199.
- (31) Zhang, Y.; Kim, S. G.; Lee, D.; Shin, H.; Park, N. G. Bifacial stamping for high efficiency perovskite solar cells. *Energy Environ. Sci.* **2019**, *12* (1), 308–321.
- (32) Li, C.; Wang, Y.; Choy, W. C. Efficient interconnection in perovskite tandem solar cells. *Small Methods* **2020**, *4* (7), No. 2000093.
- (33) Jeon, N. J.; Noh, J. H.; Kim, Y. C.; Yang, W. S.; Ryu, S.; Seok, S. I. Solvent engineering for high-performance inorganic–organic hybrid perovskite solar cells. *Nat. Mater.* **2014**, *13* (9), 897–903.
- (34) Montes-Valenzuela, I.; Pérez-Sánchez, F.; Morales-Acevedo, A. Structural, optical and photoluminescence properties of hybrid metal–organic halide perovskite thin films prepared by a single step solution method. *J. Mater. Sci.: Mater. Electron.* **2018**, *29* (18), 15404–15410.
- (35) Gordillo, G.; Otálora, C. A.; Reinoso, M. A. Trap center study in hybrid organic-inorganic perovskite using thermally stimulated current (TSC) analysis. *J. Appl. Phys.* **2017**, *122* (7), No. 075304, DOI: [10.1063/1.4999297](https://doi.org/10.1063/1.4999297).
- (36) Park, B. W.; Kedem, N.; Kulbak, M.; Lee, D. Y.; Yang, W. S.; Jeon, N. J.; Seo, J.; Kim, G.; Kim, K. J.; Shin, T. J.; Hodes, G.; Cahen, D.; Seok, S., II. Understanding how excess lead iodide precursor improves halide perovskite solar cell performance. *Nat. Commun.* **2018**, *9* (1), No. 3301.
- (37) Tulus, N.; Muscarella, L. A.; Galagan, Y.; Boehme, S. C.; Hauff, E. V. Trap passivation and suppressed electrochemical dynamics in perovskite solar cells with C₆₀ interlayers. *Electrochim. Acta* **2022**, *433*, No. 141215, DOI: [10.1016/j.electacta.2022.141215](https://doi.org/10.1016/j.electacta.2022.141215).
- (38) Wang, L.; Wang, Z.; Li, H.; Chang, B.; Pan, L.; Xie, Z.; Yin, L. Pseudohalide anions to suppress oxidative degradation for efficient formamidinium-based Sn-Pb halide perovskite solar cells. *ACS Appl. Mater. Interfaces* **2022**, *14* (16), 18302–18312.
- (39) Werner, J.; Moot, T.; Gossett, T. A.; Gould, I. E.; Palmstrom, A. F.; Wolf, E. J.; Boyd, C. C.; Van Hest, M. F. A. M.; Luther, J. M.; Berry, J. J.; McGehee, M. D. Improving low-bandgap tin–lead perovskite solar cells via contact engineering and gas quench processing. *ACS Energy Lett.* **2020**, *5* (4), 1215–1223.
- (40) Hu, M.; Bi, C.; Yuan, Y.; Bai, Y.; Huang, J. Stabilized wide bandgap MAPbBr_xI_{3-x} perovskite by enhanced grain size and improved crystallinity. *Adv. Sci.* **2015**, *3* (6), No. 1500301, DOI: [10.1002/advs.201500301](https://doi.org/10.1002/advs.201500301).
- (41) Luo, D.; Su, R.; Zhang, W.; Gong, Q.; Zhu, R. Minimizing non-radiative recombination losses in perovskite solar cells. *Nat. Rev. Mater.* **2020**, *5* (1), 44–60.
- (42) Jamieson, F. C.; Domingo, E. B.; McCarthy-Ward, T.; Heeney, M.; Stingelin, N.; Durrant, J. R. Fullerene crystallisation as a key driver of charge separation in polymer/fullerene bulk heterojunction solar cells. *Chem. Sci.* **2012**, *3* (2), 485–492.
- (43) Zhang, Y. X.; Wang, H. Y.; Zhang, Z. Y.; Zhang, Y.; Sun, C.; Yue, Y. Y.; Wang, L.; Chen, Q. D.; Sun, H. B. Photoluminescence quenching of inorganic cesium lead halides perovskite quantum dots (CsPbX₃) by electron/hole acceptor. *Phys. Chem. Chem. Phys.* **2017**, *19* (3), 1920–1926.
- (44) Kim, J.; Godin, R.; Dimitrov, S. D.; Du, T.; Bryant, D.; McLachlan, M. A.; Durrant, J. R. Excitation density dependent photoluminescence quenching and charge transfer efficiencies in hybrid perovskite/organic semiconductor bilayers. *Adv. Energy Mater.* **2018**, *8* (35), No. 1802474.
- (45) Li, X.; Zhang, W.; Guo, X.; Lu, C.; Wei, J.; Fang, J. Constructing heterojunctions by surface sulfidation for efficient inverted perovskite solar cells. *Science* **2022**, *375* (6579), 434–437.
- (46) Hutson, N. D.; Attwood, B. C.; Scheckel, K. G. XAS and XPS characterization of mercury binding on brominated activated carbon. *Environ. Sci. Technol.* **2007**, *41* (5), 1747–1752.
- (47) Kirmani, A. R.; Mansour, A. E.; Yang, C.; Munir, R.; El-Zohry, A. M.; Mohammed, O. F.; Amassian, A. Facile and noninvasive passivation, doping and chemical tuning of macroscopic hybrid perovskite crystals. *PLoS One* **2020**, *15* (3), No. e0230540.
- (48) Zhang, F.; Xiao, C.; Chen, X.; Larson, B. W.; Harvey, S. P.; Berry, J. J.; Zhu, K. Self-seeding growth for perovskite solar cells with enhanced stability. *Joule* **2019**, *3* (6), 1452–1463.
- (49) Chen, K.; Wu, P.; Yang, W.; Su, R.; Luo, D.; Yang, X.; Tu, Y.; Zhu, R.; Gong, Q. Low-dimensional perovskite interlayer for highly efficient lead-free formamidinium tin iodide perovskite solar cells. *Nano Energy* **2018**, *49*, 411–418.
- (50) Li, D.; Kong, W.; Zhang, H.; Wang, D.; Li, W.; Liu, C.; Chen, H.; Song, W.; Gao, F.; Amini, A.; Xu, B.; Li, S.; Cheng, C. Bifunctional ultrathin PCBM enables passivated trap states and cascaded energy level toward efficient inverted perovskite solar cells. *ACS Appl. Mater. Interfaces* **2020**, *12* (17), 20103–20109.
- (51) Seo, J.; Park, S.; Kim, Y. C.; Jeon, N. J.; Noh, J. H.; Yoon, S. C.; Seok, S. I. Benefits of very thin PCBM and LiF layers for solution-processed p-i-n perovskite solar cells. *Energy Environ. Sci.* **2014**, *7*, 2642–2646.
- (52) Huang, J. H.; Wei, H. Y.; Huang, K. C.; Chen, C. L.; Wang, R. R.; Chen, F. C.; Ho, K. C.; Chu, C. W. Using a low temperature crystallization process to prepare anatase TiO₂ buffer layers for air-stable inverted polymer solar cells. *Energy Environ. Sci.* **2010**, *3* (5), 654–658.
- (53) Hu, T.; Li, F.; Yuan, K.; Chen, Y. Efficiency and air-stability improvement of flexible inverted polymer solar cells using ZnO/poly(ethylene glycol) hybrids as cathode buffer layers. *ACS Appl. Mater. Interfaces* **2013**, *5* (12), 5763–5770.
- (54) Liu, C.; Yang, Y.; Rakstys, K.; Mahata, A.; Franckevicius, M.; Mosconi, E.; Skackauskaite, R.; Ding, B.; Brooks, K. G.; Usiobo, O. J.; Audinot, J. N.; Kanda, H.; Driukas, S.; Kavaliauskaitė, G.; Gulbinas, V.; Dessimoz, M.; Getautis, V.; De Angelis, F.; Ding, Y.; Dai, S.; Dyson, P. J.; Nazeeruddin, M. K. Tuning structural isomers of phenylenediammonium to afford efficient and stable perovskite solar cells and modules. *Nat. Commun.* **2021**, *12* (1), No. 6394.
- (55) Park, H.; An, J.; Song, J.; Lee, M.; Ahn, H.; Jahnel, M.; Im, C. Thickness-dependent internal quantum efficiency of narrow band-gap polymer-based solar cells. *Sol. Energy Mater. Sol. Cells* **2015**, *143*, 242–249.